I&EC research
Industrial & Engineering Chemistry Research
pubs.acs.org/IECR
Article

Reduced Aging in Carbon Molecular Sieve Membranes Derived from PIM-1 and MOP-18

Whitney K. Cosey, Kenneth J. Balkus, Jr., John P. Ferraris, and Inga H. Musselman*

Cite This: *Ind. Eng. Chem. Res.* 2021, 60, 9962−9970
Read Online

ABSTRACT: Carbon molecular sieve membranes (CMSMs) commonly lose permeability over time due to the collapse of micropores. This decline in permeability, due to the densification of the membrane, is known as physical aging. CMSMs derived from polymers of intrinsic microporosity (PIM-1) are highly affected by physical aging, with declines in permeability greater than 60% over time. It is hypothesized that the densification of CMSMs derived from this high-free-volume polymer precursor is thermodynamically driven by the collapse of large unconnected graphene domains to reach a more stable conformation (i.e., graphite). This study describes a novel strategy to mitigate physical aging by pillaring the CMSM using copper nanoparticles. Highly soluble metal−organic polyhedra-18 (MOP-18) was introduced into PIM-1 with loadings up to 40 wt/wt to form a mixed-matrix membrane (MMM). Pyrolysis of the MMM at 550 °C resulted in the in situ formation of copper metal nanoparticles that acted as pillars for the graphene sheets within the CMSM, preventing the collapse of the micropores, thus minimizing the aging of the CMSM. Single gas permeation measurements of CO_2 and CH_4 were made on the pristine polymer-derived CMSM and the copper-pillared CMSM at 35 °C and 2 bar to confirm the membranes' resistance to physical aging. The CH_4 permeability for the PIM-1 CMSM decreased by ∼60%, from 64 to 27 Barrers, over a period of 7 days, while the copper-pillared PIM-1 CMSM remarkably showed essentially no decline in CH_4 permeability. This research demonstrates a general approach to reducing physical aging in CMSMs.

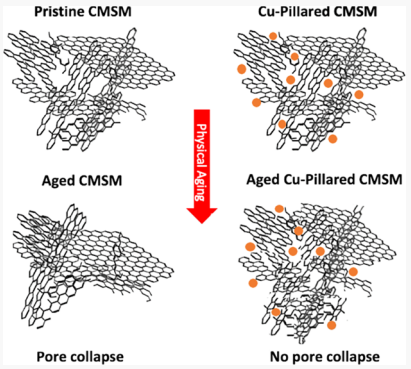

1. INTRODUCTION

Current CO_2 emissions from fossil fuels and natural gas processing make up approximately 65% of the total greenhouse gases emitted globally.[1,2] In recent years, more focus has been placed on the separation and capture of CO_2 to combat the effects of global warming. Membrane-based gas separation provides a cost-effective method to separate CO_2. However, with CO_2 emissions steadily rising each year, it is imperative that the efficiency of these separations is improved. Carbon molecular sieve membranes (CMSMs) have gained attention in this regard due to their unique pore structure and surface area.[3,4] CMSMs are composed of both ultramicropores (<0.7 nm) and micropores (0.7−2 nm), which provide the membrane with high selectivity and high permeability, respectively.[5] Their inherent pore size distribution also allows them to surpass the performance of polymeric membranes used for gas separations.[6] Despite this improved permselectivity,[4,5,7] CMSMs are subject to physical and chemical aging.[4,8−10] Chemical aging is the result of chemisorption and physisorption of unwanted species in and on the membrane, causing a decline in permeability.[11,12] In contrast, physical aging results from the collapse of the membrane pore structure and subsequent densification.[12,13] Physical aging, unlike chemical aging, cannot be reversed to regenerate the initial or "fresh" permselectivity.[11,14] Therefore, controlling the CMSM pore structure following pyrolysis has become the focus of several research groups. Altering the carbonization procedure by adjusting either the final pyrolysis temperature or the soak time allows for a reduction in physical aging; however, it also results in a subsequent decline in permeability.[15−17] This method also tends to cause a decline in the mechanical stability of the membrane, resulting in more brittle materials. A second approach that has shown promising results is to cross-link the polymer precursor prior to carbonization.[18] However, this method is dependent on, and thus limited by, the polymer's functionality. A more efficient approach would be to stabilize the pore structure of the CMSM by incorporating a support system that would remain after pyrolysis. Nakagawa and colleagues' tactic of cross-linking ion-exchange resins using metal cations provides a pathway to stabilize CMSMs by introducing metal pillars.[19] Our approach, described below, incorporates an additive into the polymer precursor, which forms metal nanoparticles after pyrolysis to pillar the pore structure, preventing the densification of the membrane. This

Received: May 6, 2021
Revised: June 8, 2021
Accepted: June 10, 2021
Published: July 5, 2021

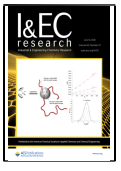

https://doi.org/10.1021/acs.iecr.1c01727
Ind. Eng. Chem. Res. 2021, 60, 9962−9970

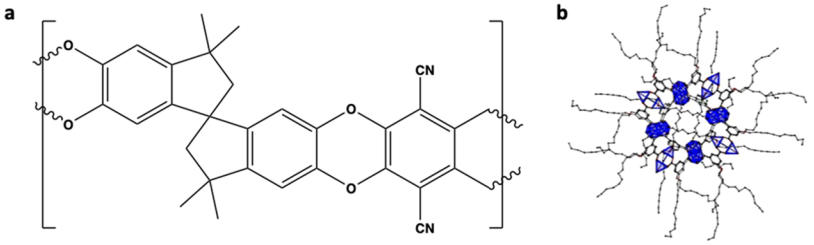

Figure 1. Chemical structures of (a) PIM-1 and (b) MOP-18. Blue represents the copper paddle wheels.

technique provides a means to reduce physical aging without sacrificing the permselectivity of the membrane. It also has the benefit of being independent of the polymer precursor's functionality, making it a more general approach to stabilizing CMSMs.

A mixed-matrix membrane (MMM) composed of metal–organic polyhedra-18 (MOP-18) and polymer of intrinsic microporosity-1 (PIM-1) was prepared.[20] The rigid backbone of PIM-1 reduces the flexibility of the polymer, preventing the polymer from packing efficiently.[21−23] This rigidity translates to an inability to stack into graphitic sheets upon carbonization, which results in turbostratic carbon with a higher content of sp^3 terminal sites. This is a common feature of CMSMs derived from high-free-volume polymers, and is accompanied by high, but unstable, permeability due to physical aging.[24,25] PIM-1 is composed of fused rings with spiro-centers as shown in Figure 1a.[21,26] MOP-18 is composed of discrete porous molecular cages, making it easily dispersed in a polymer matrix (Figure 1b).[21,27,28] MOP-18 has an alkyl chain-to-chain diameter of ∼50 Å. The center-to-center distance between neighboring polyhedra is ∼24 Å. Unlike simple metal salts, MOP-18 does not cross-link the polymer, causing it to become insoluble. This attribute allowed for higher weight loadings of MOP-18 to be achieved. The pyrolysis of the PIM-1-based MMM results in the in situ formation of copper nanoparticles, which provide a stable scaffold for the inherent pore structure of the resultant CMSM.

In this study, the CMSM was prepared by the pyrolysis of a 40 wt/wt MOP-18/PIM-1 MMM (details in the Experimental Section). This weight loading was determined to be optimal as it yielded defect-free CMSMs that were mechanically sound. We show that uniformly dispersed copper nanoparticles (CuNPs) are capable of suppressing physical aging within CMSMs. We believe that this result provides a significant contribution to the membrane field as it represents a more general approach to stabilizing CMSMs.

2. EXPERIMENTAL SECTION

2.1. Materials. PIM-1: 5,5′,6,6′-tetrahydroxy-3,3,3′,3′-tetramethyl-1,1′-spirobisindane (TTSBI) (96%, Sigma-Aldrich) was recrystallized using methanol and dichloromethane to purify the material. 1,4-Dicyanotetrafluorobenzene (DCTB) (99%, Sigma-Aldrich) was purified by vacuum sublimation at 140 °C. DMF (99.8%, Sigma-Aldrich) was dried over 4A 4-8 mesh (Sigma-Aldrich) molecular sieves, and anhydrous potassium carbonate (98%, Sigma-Aldrich) was dried at 60 °C for 1 day to ensure no water was present. Purification procedures are described in detail elsewhere.[26]

MOP-18: The following materials were purchased from Sigma-Aldrich with purities greater than 97%: sodium bicarbonate, 1-iodododecane, 5-hydroxyisophthalic acid, copper acetate monohydrate, ethyl acetate, acetonitrile, potassium hydroxide, methanol, tetrachloroethane, and chloroform. Ethyl ether (99.9%) and hydrochloric acid were purchased from J.T. Baker. Concentrated sulfuric acid was purchased from Mallinckrodt. Methanol, acetonitrile, and DMF were dried prior to use over 4A molecular sieves.

2.2. Polymer Synthesis. PIM-1 was synthesized using reported procedures.[26] Producing high-molecular-weight PIM-1 required a 1:1:2 reactant ratio, respectively, of tetrahydroxytetramethylspirobisindane (TTSBI), 1,4-dicyanotetrafluorobenzene (DCTB), and anhydrous K_2CO_3. The monomers were purified prior to synthesis as described in the Materials section. Anhydrous K_2CO_3 (4.2 g, 30 mmol), TTSBI (5.1 g, 15 mmol), and DCTB (3.0 g, 15 mmol) were dissolved in anhydrous DMF (100 mL) and magnetically stirred in a 250 mL flask. The reaction flask was sealed with a septum so that air could be removed by application of vacuum and replaced with N_2 gas; this process was repeated four times. The reaction flask was then stirred magnetically (810 rpm) at 55 °C for 23 h. Upon cooling, 150 mL of deionized water was added to the mixture and the product was collected by filtration. A 75% yield of the neon yellow polymer (PIM-1) was obtained after drying at 90 °C for 1 day (M_w 60 000 and PDI of 2 by GPC).

2.3. MOP-18 Synthesis. First, the MOP-18 linker, 5-dodecoxyisophthalic acid, was prepared by esterifying 5-hydroxyisophthalic acid with ethanol. Alkylation of the hydroxyl group of the diester, followed by hydrolysis, yielded 5-dodecoxyisophthalic acid. Then, two solutions were prepared. The linker (2.7 g) was dissolved in 100 mL of hot (80 °C) DMF and stirred until a clear solution was obtained. Copper acetate (1.5 g) was dissolved in 50 mL of DMF and stirred at room temperature until fully dissolved. The two solutions were combined, and 100 mL of methanol was added. The precipitate was allowed to crystallize for 24 h at room temperature, and then was washed 2× with methanol, filtered, and dried in a vacuum oven at 60 °C for 24 h to yield blue MOP-18 crystals (93% yield). A more detailed synthesis may be found elsewhere.[20,27]

2.4. Fabrication of Precursor Polymeric Membranes. Solutions for 40 wt/wt MOP-18/PIM-1 MMMs were prepared by first dissolving 0.5 g of PIM-1 in 4 g of $C_2H_2Cl_4$ and 0.2 g of MOP-18 in 3 g of $C_2H_2Cl_4$ in separate scintillation vials. These solutions were stirred for 24 h and then combined. The combined solution was stirred for an additional 24 h. After thorough mixing (clear blue/green solution), the solution was concentrated by evaporating solvent until the polymer concentration reached 15 wt %. Pristine PIM-1 membranes were prepared by dissolving 0.5 g of PIM-1 in 3.3 g $C_2H_2Cl_4$. The solution was stirred for 24 h at room temperature. A Sheen 1133N automatic applicator with a doctor blade was used to cast the membranes onto a glass substrate. After 48 h, the membranes were carefully removed using methanol and annealed in a vacuum oven at 150 °C for 1 day. The average

https://doi.org/10.1021/acs.iecr.1c01727
Ind. Eng. Chem. Res. 2021, 60, 9962−9970

thickness of the 40 wt/wt MOP-18/PIM-1 MMMs and pristine PIM-1 films was 90 μm.

2.5. Formation of Carbon Molecular Sieve Membranes. The CMSMs were formed by pyrolysis of flat precursor PIM-1 membranes and MMMs. A three-zone tube furnace (MSI-1200X-III) with a quartz tube (National Scientific Company, GE Type 214 Quartz) was fitted with a PID temperature controller (Omega Engineering, Inc., model CN1507TC). Precursor membranes were placed on a graphite plate inside the quartz tube. Pyrolysis was carried out using the temperature protocol displayed below under a continuous flow of ultrahigh-purity nitrogen (UHP, 200 cm^3/min). The CMSMs were removed from the furnace after cooling to room temperature under nitrogen and characterized.

Carbonization Protocol[8]

1. 20−250 °C at a ramp rate of 15 °C/min
2. 250−535 °C at a ramp rate of 3.85 °C/min
3. 535−550 °C at a ramp rate of 0.25 °C/min
4. 120 min soak at 550 °C

2.6. Characterization. *2.6.1. Polymer.* The molecular weight and molecular-weight distribution of PIM-1 were characterized by size-exclusion chromatography (SEC) using a Viscotek VE 3580 system equipped with a Viscotek column (T6000M) and ultraviolet−visible (UV−vis) detector. The SEC solvent/sample module (GPCmax) used high-performance liquid chromatography (HPLC)-grade THF as the eluent, and calibration was based on polystyrene standards.

2.6.2. Membrane. Cross sections of polymer membranes were imaged using a Zeiss SUPRA 40 scanning electron microscope (SEM). Polymer membrane cross sections were prepared by freeze-fracturing the samples submerged in liquid nitrogen. Thermogravimetric analysis (TGA) of the polymer membranes was completed using a PerkinElmer Pyris 1 TGA thermogravimetric analyzer under a UHP N_2 flow (20 cm^3/min) and a ramp rate of 10 °C/min. A Nicolet 360 FTIR instrument equipped with a diamond crystal single-bounce ATR attachment was used to acquire attenuated total reflectance-Fourier transform infrared (ATR-FTIR) spectra of the polymer films.

2.6.3. CMSM. Raman analysis of the CMSMs was performed using a DXR Raman spectrophotometer with a 532 nm laser. X-ray diffraction analysis of the CMSMs as well as MOP-18 was accomplished using a Rigaku Ultima III diffractometer with Cu Kα X-ray radiation. X-ray photoelectron spectroscopy (XPS) of the CMSMs was performed at $\leq 5 \times 10^{-10}$ mbar using a PHI VersaProbe II with Al Kα (1486.7 eV) as the X-ray source. Spectra were acquired using a pass energy of 23.5 eV and a step energy of 0.1 eV and with charge compensation using an electron beam positioned incident to the sample. Spectra were collected before and after sputtering for 2 min using a gas cluster ion beam at 20 kV with a 2 × 2 mm^2 spot size to ensure oxygen was removed from the surface. All spectra were then analyzed using CasaXPS software.

Atomic force microscopy (AFM) of carbon membranes was performed using a Bruker Multimode 8 AFM with a Nanoscope V controller, Nanoscope 8.1 software, and RTESPA 525A probes. Samples were mounted on magnetic stainless steel disks using double-sided carbon tape (Ted Pella, Inc.). AFM imaging was carried out at 1 kHz frequency, 0.5 Hz scan rate, and 150 nm amplitude at a sample indentation depth of 2 nm. To measure mechanical properties, the probe's deflection sensitivity was calibrated using a fused silica standard (72 GPa). Then, the values for the probe's spring constant and tip radius were manually adjusted while imaging a polystyrene calibration standard until the modulus channel displayed a Young's modulus value of 2.9 GPa at 2 nm probe indentation (polystyrene's literature value for Young's modulus). Subsequently, relative Young's modulus values of CMSM samples were obtained by imaging samples at a 2 nm indentation using the same probe. The probe's radius was monitored throughout the experiment to ensure its size and shape (and thus, the calibration) were maintained.

2.6.4. Cu Particles. A JEOL 1400+ transmission electron microscope (TEM) operating at 200 kV was used to image the copper particles present within the CMSM. Samples for TEM were prepared by micronizing the flat carbon membranes using a Resodyn LabRAM Acoustic Mixer at 30 G for 30 min. The powder was then dispersed in methanol. Copper particles were adhered to stainless steel grids (200 mesh, Ted Pella) by immersing the grids in the methanol solution. The sizes of the copper particles in the TEM images were quantified using ImageJ.

2.6.5. Gas Permeability Testing. The pure gas permeability of each membrane was determined using custom-built permeameters with a LabVIEW 16.0 software interface (National Instruments), previously described by Perez et al.[29] Flat membranes with known surface areas and thicknesses were mounted into permeation cells and degassed for 12 h before testing at 35 °C. A gas leak test was also performed prior to each experiment to ensure accurate permeabilities were obtained. During these experiments, the upstream side of the permeation cell was maintained at 35 °C and 2 bar with the respective gas (CO_2 or CH_4 in this study). Pressure transducers were used to monitor the upstream and downstream pressures over time. Equation 1 was used to calculate the permeability of each membrane, utilizing permeability of gas (P_i), flux of gas (n_i), thickness of the membrane (l), and the transmembrane partial pressure difference (Δp_i).[30] Ideal selectivity was calculated using the permeability ratio of carbon dioxide (P-CO_2) and methane (P-CH_4) for each membrane.

$$P_i = \frac{(n_i)(l)}{\Delta p_i} \tag{1}$$

2.6.6. Aging Experiments. The apparatus described above (gas permeability testing) was used for these measurements. Membranes remained in the permeation cell for the entire duration of the experiment. The aging of a membrane was performed by evacuating both the upstream and downstream sides of the membrane for extended periods of time (1 day, 2 days, etc.). Between each run of the same gas, the upstream and downstream sides were degassed for 4 h to remove adsorbed gas molecules. The aging experiments for both the Cu-pillared CMSM and the PIM-1 derived CMSM lasted 21 days.

2.6.7. Mixed Gas Experiments. A custom-built permeameter[31] in conjunction with an SRI-3610 gas chromatograph (GC) equipped with a thermal conductivity detector was used for mixed gas (carbon dioxide/methane = 50:50) experiments. Calibration of the GC was carried out by injecting pure CO_2 and CH_4 samples at pressures between 0.01 and 1.0 bar into the sampling loop. The detector signal versus pressure was plotted to obtain the calibration curves. Prior to each experiment, the upstream and downstream sides of the permeation cell were degassed for 12 h. A gas leak test

https://doi.org/10.1021/acs.iecr.1c01727
Ind. Eng. Chem. Res. 2021, 60, 9962−9970

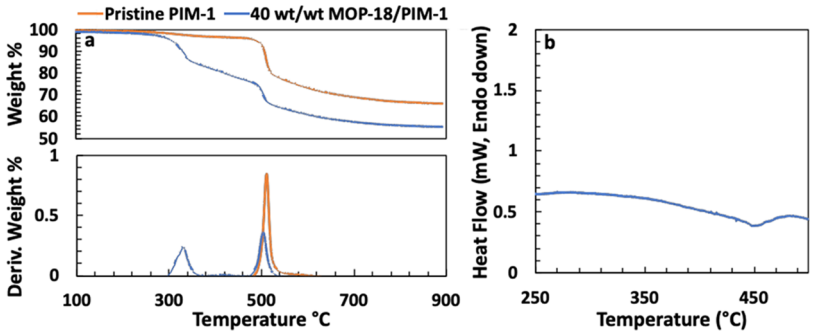

Figure 2. (a) TGA and derivative TGA curves of pristine PIM-1 (orange) and 40 wt/wt MOP-18/PIM-1 MMM (blue). (b) DSC curve of 40 wt/wt MOP-18/PIM-1 MMM.

performed prior to each experiment revealed leak rates of less than 0.04 mbar/h. For mixed gas experiments, the cell was maintained at 35 °C with an upstream pressure of 3.0 bar. Pressure transducers were used to monitor the upstream and downstream pressures over time. A stage cut (Ø) (eq 2) of 0.1 was used for this experiment by determining the retentate purge rate (Q_R). This was calculated using the mixed gas flow rate across the membrane (Q_P) without a stage cut.[31] The retentate purge rate was controlled by a mass flow controller connected to the feed side.

$$Ø = \frac{(Q_P)}{(Q_P + Q_R)} \quad (2)$$

Upon obtaining sufficient pressure in the downstream side, the permeate was then injected into the GC (500 Torr). The mixed gas selectivity was acquired by calculating the ratio of the detector signals for each gas using their calibration curves. The permeabilities for CO_2 and CH_4 were then back-calculated from the experimentally determined selectivity.

3. RESULTS AND DISCUSSION

3.1. In Situ Formation of CuNPs. Thermal analysis of the pristine PIM-1 and 40 wt/wt MOP-18/PIM-1 MMMs showed a major weight loss of 40% at 500 °C due to the decomposition of PIM-1. The MMM also exhibited a smaller weight loss of 20% at 260 °C due to the decomposition of the coordinating linkers of MOP-18 (Figure 2a).[32] The weight loss observed at 500 °C for both membranes suggests that the incorporation of MOP-18 into the matrix does not reduce the membranes' thermal stability. Upon the thermal degradation of MOP-18 at 260 °C, copper nanoparticles are formed in situ. The melting temperature of these nanoparticles was determined using DSC.[33] Figure 2b shows a melting temperature near 450 °C for the copper particles present within the CMSM, which agrees with theoretical calculations for copper particles less than 20 nm.[34−36] Particles less than 20 nm are known to show a depressed melting temperature in comparison to the melting temperature of the bulk metal (Cu^0, 1083 °C) and play a role in the ability of nanoparticles to agglomerate.[34−36] The instantaneous formation of particles after reaching 260 °C, along with diffusion-controlled growth when in the liquid phase, influences the average size of particles.[37] Therefore, parameters such as the pyrolysis temperature, soaking duration, and polymeric precursor (free-volume content) allow for control over the size distribution of the copper nanoparticles.

3.2. Tuning Cu Particle Size Distribution. Transmission electron microscopy (TEM) of the copper nanoparticles shows an average particle diameter between 1 and 20 nm with an aspect ratio of 1 (Figure 3a−c). The particle size distribution

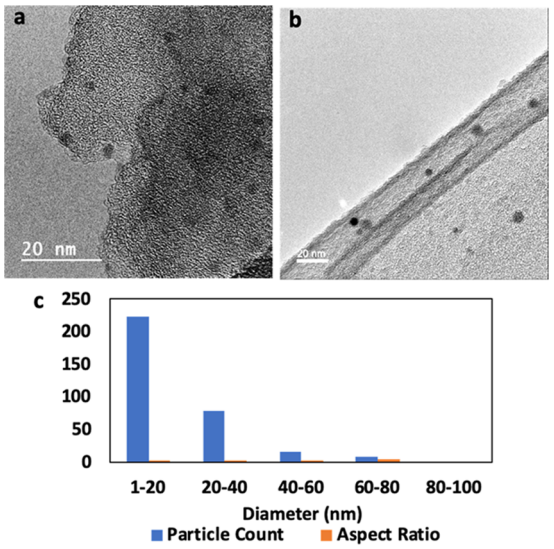

Figure 3. (a, b) TEM images of 40 wt/wt MOP-18/PIM-1 CMSM and (c) its corresponding histogram.

obtained suggests that agglomeration of the copper particles was impeded after approaching 20 nm. This is due to the drastic increase in Tm of the larger particles (>20 nm), minimizing diffusion-controlled growth. Particles>20 nm are a result of Ostwald ripening, which dictates that the larger particles will grow at the expense of the smaller ones.[38] Thus, interactions due to the disruptive pyrolysis procedure can bring about a growth in particle size. Minimizing agglomeration is a key factor in obtaining copper nanoparticles with sizes less than 10 nm. The size range obtained after pyrolysis of the MMM at 550 °C yielded copper nanoparticles which proved to be optimal for this high-free-volume system. The turbostratic carbon produced, as well as its resultant degree of disorder, will be discussed further in the following section.

Figure 4 shows an X-ray diffraction pattern for a 40 wt/wt MOP-18/PIM-1 CMSM with three peaks at 2θ = 43, 50, and 74° corresponding to the 111, 200, and 220 reflections of copper metal. A crystallite size of 14 nm was calculated by applying the Scherrer equation (eq 3), where D_p is the average crystallite size, λ is the X-ray wavelength (Cu Kα), and β is line broadening in radians (peak full width at half-maximum,

https://doi.org/10.1021/acs.iecr.1c01727
Ind. Eng. Chem. Res. 2021, 60, 9962−9970

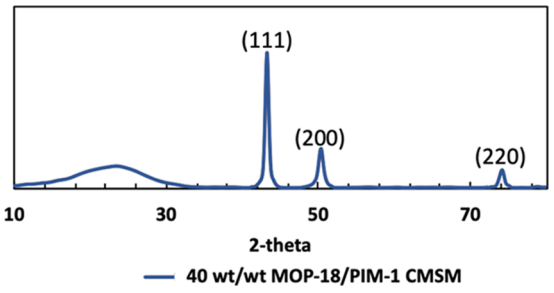

Figure 4. X-ray diffraction pattern of a 40 wt/wt MOP-18/PIM-1-derived CMSM.

FWHM). The value calculated (14 nm) agrees with the TEM images shown in Figure 3.

$$D_p = \frac{(0.94\lambda)}{(\beta \cos \theta)} \quad (3)$$

3.3. Impact of Turbostratic Carbon on CMSM Stability. Raman spectroscopy provides a convenient tool to predict the rate of decline in permeability due to physical aging as well as its underlying causes. The Raman spectrum of crystalline graphite is defined by the presence of two strong peaks labeled disorder (D-band) and graphitic (G-band) at 1350 and 1580 cm^{-1}, respectively.[39] The height ratio of the D-band to G-band provides a measure of disorder within the sp^2–sp^3-bonded carbons. Based on eq 4, the I_D/I_G ratio can be used to determine the graphite crystallite size (L_a), where L_a is inversely proportional to the I_D/I_G ratio.[40] When a CMSM is determined to have a small crystallite size (or a high I_D/I_G ratio), which is typically observed when high-free-volume polymer precursors are pyrolyzed, the CMSM usually has high flux. The observed increase in flux, in comparison to a CMSM composed of large crystallites, is due to the inefficient stacking of sp^3 terminal carbons in the small graphite domains, which generate pores. The G-band position can also be used to monitor changes in disorder associated with graphitic carbon.[39,41] A blueshift in the G-band corresponds to an increase in sp^3 carbons as well as to a transition from sp^2 carbon rings to sp^2 carbon chains.[39,41]

$$L_a = 44(I_D/I_G)^{-1} \quad (4)$$

Raman analysis was used to determine the effect that the 12-C chain of MOP-18 has on the graphitic nature of the CMSM. As shown in Figure 5a, the I_D/I_G ratio of pyrolyzed PIM-1 is 0.94. The small unconnected domains are hypothesized to be the reason behind the rapid aging of PIM-1. However, upon incorporation of MOP-18, a 0.12 decrease in the I_D/I_G ratio is observed (Figure 5c). This decrease is most likely due to the carbon associated with MOP-18 as the pyrolysis of MOP-18 itself yields a fairly graphitic material (Figure 5b, I_D/I_G = 0.72). This secondary source of graphitic carbon in the 40 wt/wt MOP-18/PIM-1-derived CMSM (Figure 5c) may be a factor contributing to the stabilization of the carbon membrane. The increase in graphite crystallite size for the pillared CMSM (L_a = 5.4 nm), compared to that for the PIM-1-derived CMSM (L_a = 4.7 nm), corresponds to a reduction in the number of terminal sp^3 carbon sites,[42] which may minimize distortions in the CMSM. When comparing the pristine derived PIM-1 CMSM to the 40 wt/wt MOP-18/ PIM-1 CMSM, a redshift in the G-band position from 1590 to 1585 cm^{-1} is observed. This suggests that the Cu-pillared CMSM is more stable than PIM-1 because it has fewer sp^3 carbons. The data acquired from Raman analysis are summarized in Table 1. Averages were obtained from three separate CMSMs.

While stabilizing graphitic sheets by means of increasing the crystallite size, and thus decreasing distortions due to sp^3 terminal carbons is important, it should be stated that this alone is not sufficient to eliminate physical aging. For example, Xu et al. showed a decline in ethylene permeance by 40% over a period of 6 days for a Matrimid 5218-derived CMSM that was pyrolyzed at 550 °C.[12] The Matrimid 5218-derived CMSM had an I_D/I_G ratio of 0.6 and a corresponding

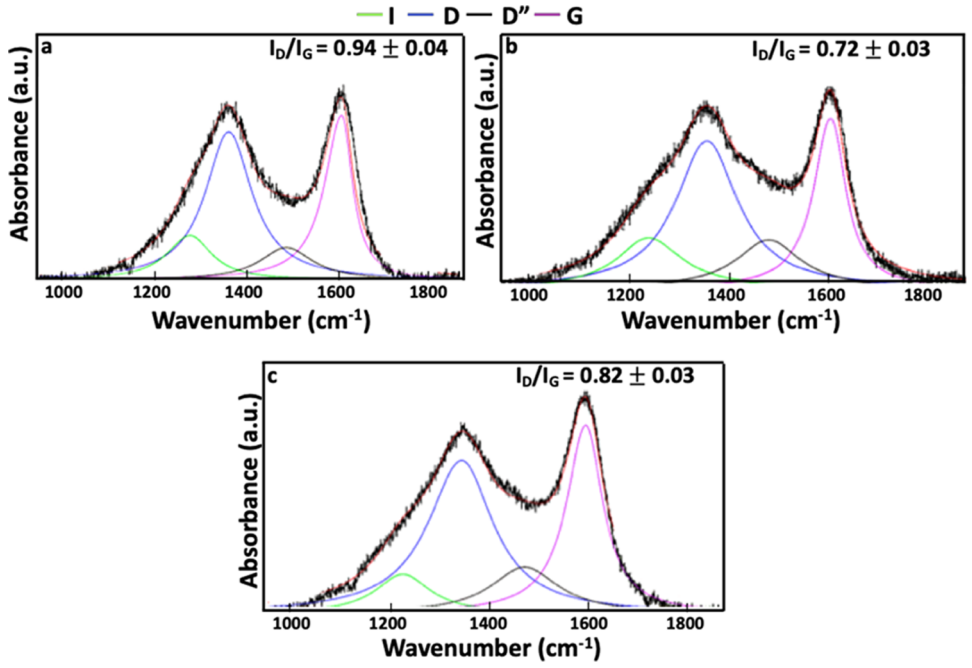

Figure 5. Raman spectra of carbon: (a) PIM-1, (b) MOP-18, and (c) 40 wt/wt MOP-18/PIM-1.

https://doi.org/10.1021/acs.iecr.1c01727
Ind. Eng. Chem. Res. 2021, 60, 9962−9970

Table 1. I_D/I_G Height Ratios, Corresponding L_a Values, and G-band Positions for PIM-1, MOP-18, and 40 wt/wt MOP-18/PIM-1 Pyrolyzed at 550 °C

carbon source	I_D/I_G (height)	L_a (nm)	G-band (cm^{-1})
PIM-1	0.94 ± 0.04	4.7	1590
MOP-18	0.72 ± 0.03	6.1	1588
40 wt/wt MOP-18/PIM-1	0.82 ± 0.03	5.4	1585

crystallite size of 7.3 nm. Therefore, while CMSMs with larger crystallite sizes derived from low-free-volume polymer precursors may not show declines in permeability >60%,[12] as observed for high-fractional-free-volume polymer precursors, they are still subject to physical aging. Therefore, by increasing the graphite crystallite size along with the incorporation of copper pillars, physical aging within the CMSM can be impeded. The Cu nanoparticles derived from MOP-18 pillar the graphene domains of the CMSM rather than the residual carbon of MOP-18. Only 6% of the char yield for the 40 wt/wt MOP-18/PIM-1 CMSM is due to the graphitic carbon associated with MOP-18. The porosity of pyrolyzed MOP-18 was attempted to be measured by N_2 adsorption; however, essentially no porosity and surface area were detected, making it unlikely that the carbon associated with MOP-18 is being pillared.

3.4. Stability Measurements of CMSMs over Time. A universally accepted upper bound for CMSM performance has yet to be reported for any gas pair. However, the Robeson upper bound for polymers[43] allows researchers to compare carbon membrane systems with their polymer precursors. Figure 6a shows a plot of CO_2/CH_4 selectivity versus CO_2 permeability for carbon membranes that target CO_2/CH_4 separations. A 40 wt/wt MOP-18/PIM-1-derived CMSM that was aged for 21 days under vacuum (details in the Supporting Information) not only shows enhanced permselectivity values in comparison to CMSMs reported in the literature but also displays resistance to physical aging.

Figure 6b shows a plot of CO_2/CH_4 selectivity versus CO_2 permeability for fresh (▲) and aged (red triangle up open) PIM-1-derived CMSMs along with fresh (■) and aged (red box) 40 wt/wt MOP-18/PIM-1-derived CMSMs. The Cu-pillared CMSM astonishingly showed minimal change in permselectivity. This is a drastic improvement over the ∼60% decline in methane permeability observed for the pristine PIM-1-derived CMSM. The retention in permeability and selectivity are in stark contrast to other CMSMs whose permeability declines over time due to physical aging.[18,47,48]

Table 2 summarizes the pure gas permeabilities of fresh and aged CMSMs (aging protocol in the Methods section). Average permeabilities and standard deviations were calculated from one piece each of two different membranes. Each membrane surpassed the upper bound, with the Cu-pillared CMSMs showing not only enhanced permeability but also enhanced resistance to physical aging. The enhanced permeability is attributed to the incorporation of MOP-18. The free space the additive occupied prior to pyrolysis may affect the stacking of the graphitic domains within the CMSM. However, due to the relative percentage of MOP-18 (8%) within the CMSM, the Cu-pillared membrane's selectivity was not impeded.

3.5. Performance of CMSMs in a Mixed Gas. While pure gas permeability values and ideal selectivities provide research labs with a means to compare membranes based on

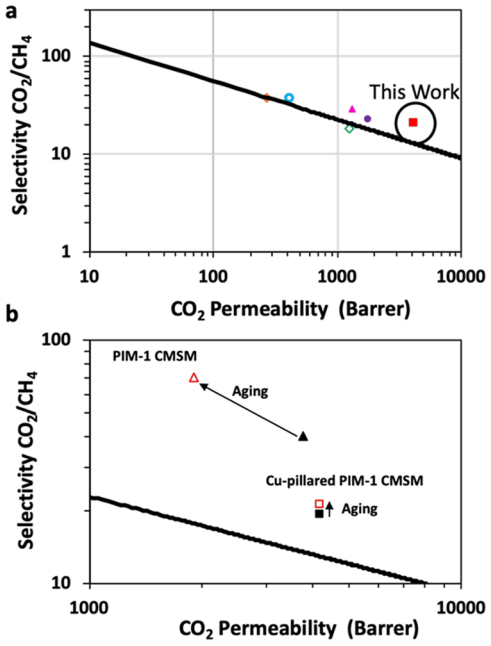

Figure 6. (a) Plot of CO_2/CH_4 selectivity versus CO_2 permeability for a 21-day-aged 40 wt/wt MOP-18/PIM-1 CMSM (red box solid), alongside CMSMs reported in the literature on Robeson's CO_2/CH_4 upper bound.[40] PBI/Matrimid (pink triangle up solid),[44] PBI/UIP-S (blue circle open),[44] P84 (purple circle solid),[45] 6FDA/PMDA-TMMDA (yellow tilted square solid),[46] and PIM-PI (green tilted square open).[47] (b) Plot of CO_2/CH_4 selectivity versus CO_2 permeability for fresh (■) and aged (red box) 40 wt/wt MOP-18/PIM-1 CMSMs alongside fresh (▲) and aged (red triangle up open) PIM-1-derived CMSMs.

the Robeson upper bounds,[43] mixed gas permselectivities reflect results that are obtained under industrially relevant conditions. The 40 wt/wt MOP-18/PIM-1 CMSM under a 50:50 mixture of CO_2 and CH_4 yielded a selectivity of 20, with methane and carbon dioxide permeabilities of 191 and 4121 Barrers, respectively (Figure 7b, Table 3). There are few articles in the literature that discuss the effects that environmental conditions have on the rate of physical aging (e.g., in air, under vacuum, under pressure gradient, etc.).[49,50] Interestingly, the results shown in Figure 7a,b reveal that the pillared CMSM maintains its permselectivity values under both vacuum and a pressure gradient, which is most similar to real-world conditions. When comparing pure gas permeabilities to mixed gas permeabilities, the data acquired were identical (Figure 7) showing no decline in permeability. Unlike polymer membranes, the CMSM investigated had very little residual functionality as shown with XPS (Supporting Information Figure S3). The gas transport is believed to be driven primarily by molecular sieving as is observed with porous graphene membranes.[51] Theoretical models confirm that the formation of size-selective pores within graphene yields a membrane with superior permselectivity, in comparison to pristine graphene.[52] The unique pore size distribution of the CMSM investigated allowed for size-selective diffusion of CO_2 and CH_4, yielding similar permselectivity values for both pure and mixed gas experiments as is observed with other graphene membranes.[53,54] These results indicate that competitive sorption, which often causes a decline in mixed gas permeability in comparison to pure gas permeability, is not a primary factor for the CMSM investigated.

https://doi.org/10.1021/acs.iecr.1c01727
Ind. Eng. Chem. Res. 2021, 60, 9962−9970

Table 2. Pure Gas Permeabilities (in Barrers) at 35 °C and 2 Bar of Fresh and Aged Carbon Molecular Sieve Membranes

membrane source	fresh P-CH_4 (Barrers) (%)	fresh P-CO_2 (Barrers) (%)	fresh CO_2/CH_4 α	aged P-CH_4 (Barrers) (%)	aged P-CO_2 (Barrers) (%)	aged CO_2/CH_4 α
40 wt/wt MOP-18/PIM-1	215 ± 4	4167 ± 4	19	200 ± 2	4187 ± 1	21
PIM-1	64 ± 10	3297 ± 5	52	27 ± 0	1902 ± 1	70

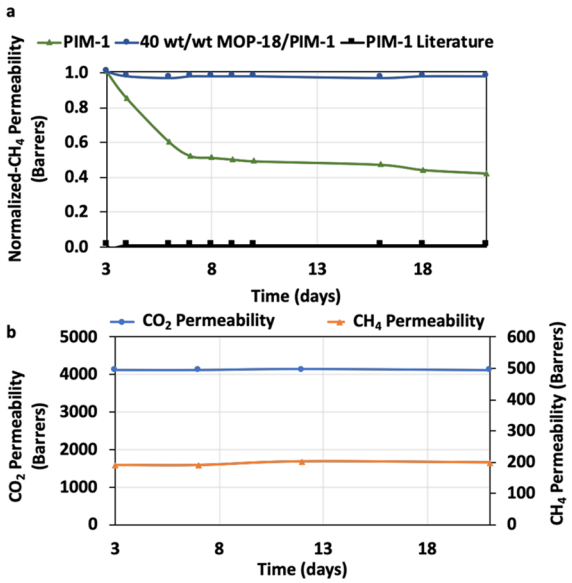

Figure 7. (a) Plot of normalized methane permeability versus time acquired under vacuum and (b) plot of CO_2 and CH_4 permeability versus time acquired under a pressure gradient with a 50:50 CO_2/CH_4 gas mixture. (a) 40 wt/wt MOP-18/PIM-1 (blue), PIM-1 bulk (green), PIM-1 submicron (black, from the literature[47]); (b) CO_2 permeability (blue) and CH_4 permeability (orange) of 40 wt/wt MOP-18/ PIM-1 CMSM.

3.6. Aging Resistance of CMSMs. Physical aging impedes carbon molecular sieve membranes from reaching their full potential.[4,12] As shown in Table 2 (fresh vs aged), physical aging is characterized by a decline in permeability and an increase in selectivity due to the collapse of the pore structure.[9,31] We have found that pillaring with copper nanoparticles produces aging-resistant carbon membranes. Figure 7 shows aging studies of pristine PIM-1-derived and 40 wt/wt MOP-18/PIM-1 MMM-derived CMSMs. The pillared CMSM (shown in blue, Figure 7a) remains stable over time, whereas the pore structure of the pristine PIM-1 CMSM (shown in green, Figure 7a) collapses after 6 days, resulting in a loss of permeability. The aging data can be compared to permeability values found in the literature for ultrathin PIM-1 CMSMs (shown in black, Figure 7a).[47] While it is known that thinner (submicron) membranes age the quickest,[24,47] the decline in permeability for the bulk PIM-1 CMSM (90 μm) used in this study still showed a decline of greater than 60% in less than 1 week. This decline was not observed for the Cu-pillared CMSM, where the resistance to physical aging is attributed to the copper nanoparticles creating a scaffold for the membrane's pore structure. The novel approach described in this study allows for the CMSM to be stabilized against physical aging without sacrificing permeability.

4. CONCLUSIONS

For the first time, copper metal nanoparticles derived from the pyrolytic carbonization of MOP-18 in PIM-1 have been used as pillars to prevent physical aging in CMSMs. The pyrolysis of the precursor MMM yielded copper nanoparticles with sizes between 1 and 20 nm, which served as a scaffold for the highly porous CMSM. DSC confirmed the melting temperature of copper to be 450 °C, which affirms the size distribution measured from TEM images. Single gas permeation data revealed that the copper-pillared CMSM displayed enhanced resistance to physical aging in comparison to pristine PIM-1-derived CMSM. The reduction in permeability of PIM-1-derived CMSMs is hypothesized to be caused by the collapse of unconnected domains. Thus, the copper pillars preserve the micropore structure of the CMSM, resulting in carbon membranes that resist physical aging while maintaining permselective performance. If this promising method is successful for other polymer systems, then it could prove to be a powerful approach to mitigate physical aging while maintaining the membranes' fresh permselectivity.

■ ASSOCIATED CONTENT

Supporting Information

The Supporting Information is available free of charge at https://pubs.acs.org/doi/10.1021/acs.iecr.1c01727.

FTIR, SEM, and XPS analyses of membranes (PDF)

■ AUTHOR INFORMATION

Corresponding Author

Inga H. Musselman − *Department of Chemistry and Biochemistry, The University of Texas at Dallas, Richardson, Texas 75080, United States*; Email: Inga.Musselman@utdallas.edu

Authors

Whitney K. Cosey − *Department of Chemistry and Biochemistry, The University of Texas at Dallas, Richardson, Texas 75080, United States*; orcid.org/0000-0002-8795-4776

Kenneth J. Balkus, Jr. − *Department of Chemistry and Biochemistry, The University of Texas at Dallas, Richardson, Texas 75080, United States*; orcid.org/0000-0003-1142-3837

Table 3. Mixed Gas Permeabilities (in Barrers) at 35 °C and 3 Bar of a 40 wt/wt MOP-18/PIM-1 Carbon Molecular Sieve Membrane

membrane source	fresh P-CH_4 (Barrers)	fresh P-CO_2 (Barrers)	fresh CO_2/CH_4 α	aged P-CH_4 (Barrers)	aged P-CO_2 (Barrers)	aged CO_2/CH_4 α
40 wt/wt MOP-18/PIM-1	191	4121	20	200	4119	21

https://doi.org/10.1021/acs.iecr.1c01727
Ind. Eng. Chem. Res. 2021, 60, 9962−9970

John P. Ferraris − *Department of Chemistry and Biochemistry, The University of Texas at Dallas, Richardson, Texas 75080, United States;* orcid.org/0000-0002-3225-0093

Complete contact information is available at: https://pubs.acs.org/10.1021/acs.iecr.1c01727

Author Contributions

W.K.C. synthesized all materials and carried out all characterization and testing.

Funding

Financial support from the NSF (CBET-1917747) is gratefully acknowledged.

Notes

The authors declare no competing financial interest.

■ ACKNOWLEDGMENTS

The technical assistance of Dr. Edson Perez is gratefully acknowledged. Dr. Melissa Wunch is acknowledged for performing XPS analysis. Charles Holt is acknowledged for performing AFM analysis.

■ REFERENCES

(1) Koytsoumpa, E. I.; Bergins, C.; Kakaras, E. The CO_2 economy: Review of CO_2 capture and reuse technologies. *J. Supercrit. Fluids* **2018**, *132*, 3−16.

(2) Withey, P.; Johnston, C.; Guo, J. Quantifying the global warming potential of carbon dioxide emissions from bioenergy with carbon capture and storage. *Renewable Sustainable Energy Rev.* **2019**, *115*, No. 109408.

(3) Jiang, L. Y.; Chung, T.-S.; Rajagopalan, R. Dual-layer hollow carbon fiber membranes for gas separation consisting of carbon and mixed matrix layers. *Carbon* **2007**, *45*, 166−172.

(4) HÄGG, M.-B.; Lie, J. A.; LINDBRÅTHEN, A. Carbon molecular sieve membranes. *Ann. N.Y. Acad. Sci.* **2003**, *984*, 329−345.

(5) Tanco, M. L.; Tanaka, D. P. Recent advances on carbon molecular sieve membranes (CMSMs) and reactors. *Processes* **2016**, *4*, No. 29.

(6) Lee, P.-S.; Kim, D.; Nam, S.-E.; Bhave, R. R. Carbon molecular sieve membranes on porous composite tubular supports for high performance gas separations. *Microporous Mesoporous Mater.* **2016**, *224*, 332−338.

(7) Sazali, N.; Salleh, W. N. W.; Ismail, A. F.; Ismail, N. H.; Yusof, N.; Aziz, F.; Jaafar, J.; Kadirgama, K. Influence of intermediate layers in tubular carbon membrane for gas separation performance. *Int. J. Hydrogen Energy* **2019**, *44*, 20914−20923.

(8) Adams, J. S.; Itta, A. K.; Zhang, C.; Wenz, G. B.; Sanyal, O.; Koros, W. J. New insights into structural evolution in carbon molecular sieve membranes during pyrolysis. *Carbon* **2019**, *141*, 238−246.

(9) Staiger, C. L.; Pas, S. J.; Hill, A. J.; Cornelius, C. J. Gas separation, free volume distribution, and physical aging of a highly microporous spirobisindane polymer. *Chem. Mater.* **2008**, *20*, 2606−2608.

(10) Lagorsse, S.; Magalhães, F. D.; Mendes, A. Aging study of carbon molecular sieve membranes. *J. Membr. Sci.* **2008**, *310*, 494−502.

(11) Menendez, I.; Fuertes, A. B. Aging of carbon membranes under different environments. *Carbon* **2001**, *39*, 733−740.

(12) Xu, L.; Rungta, M.; Hessler, J.; Qiu, W.; Brayden, M.; Martinez, M.; Barbay, G.; Koros, W. J. Physical aging in carbon molecular sieve membranes. *Carbon* **2014**, *80*, 155−166.

(13) Lagorsse, S.; Campo, M. C.; Magalhães, F. D.; Mendes, A. Water adsorption on carbon molecular sieve membranes: Experimental data and isotherm model. *Carbon* **2005**, *43*, 2769−2779.

(14) Tseng, H.-H.; Zhuang, G.-L.; Lin, M.-D.; Chang, S.-H.; Wey, M.-Y. The influence of matrix structure and thermal annealing-hydrophobic layer on the performance and durability of carbon molecular sieving membrane during physical aging. *J. Membr. Sci.* **2015**, *495*, 294−304.

(15) Geiszler, V. C.; Koros, W. J. Effects of polyimide pyrolysis conditions on carbon molecular sieve membrane properties. *Ind. Eng. Chem. Res.* **1996**, *35*, 2999−3003.

(16) Centeno, T. A.; Vilas, J. L.; Fuertes, A. B. Effects of phenolic resin pyrolysis conditions on carbon membrane performance for gas separation. *J. Membr. Sci.* **2004**, *228*, 45−54.

(17) Yoshimune, M.; Haraya, K. Flexible carbon hollow fiber membranes derived from sulfonated poly(phenylene oxide). *Sep. Purif. Techol.* **2010**, *75*, 193−197.

(18) Karunaweera, C.; Musselman, I. H.; Balkus, K. J., Jr; Ferraris, J. P. Fabrication and characterization of aging resistant carbon molecular sieve membranes for C3 separation using high molecular weight crosslinkable polyimide, 6FDA-DABA. *J. Membr. Sci.* **2019**, *581*, 430−438.

(19) Nakagawa, H.; Watanabe, K.; Harada, Y.; Miura, K. Control of micropore formation in the carbonized ion exchange resin by utilizing pillar effect. *Carbon* **1999**, *37*, 1455−1461.

(20) Lu, Z.; Knobler, C. B.; Furukawa, H.; Wang, B.; Liu, G.; Yaghi, O. M. Synthesis and structure of chemically stable Metal−Organic Polyhedra. *J. Am. Chem. Soc.* **2009**, *131*, 12532−12533.

(21) Mason, C. R.; Maynard-Atem, L.; Heard, K. W. J.; Satilmis, B.; Budd, P. M.; Friess, K.; Lanč, M.; Bernardo, P.; Clarizia, G.; Jansen, J. C. Enhancement of CO_2 affinity in a polymer of intrinsic microporosity by amine modification. *Macromolecules* **2014**, *47*, 1021−1029.

(22) Kim, H. J.; Kim, D.-G.; Lee, K.; Baek, Y.; Yoo, Y.; Kim, Y. S.; Kim, B. G.; Lee, J.-C. A carbonaceous membrane based on a polymer of intrinsic microporosity (PIM-1) for water treatment. *Sci. Rep.* **2016**, *6*, No. 36078.

(23) Mitra, T.; Bhavsar, R. S.; Adams, D. J.; Budd, P. M.; Cooper, A. I. PIM-1 mixed matrix membranes for gas separations using cost-effective hypercrosslinked nanoparticle fillers. *Chem. Commun.* **2016**, *52*, 5581−5584.

(24) Ogieglo, W.; Furchner, A.; Ma, X.; Hazazi, K.; Alhazmi, A. T.; Pinnau, I. Thin composite carbon molecular sieve membranes from a polymer of intrinsic microporosity precursor. *ACS Appl. Mater. Interfaces* **2019**, *11*, 18770−18781.

(25) Salinas, O.; Ma, X.; Litwiller, E.; Pinnau, I. Ethylene/ethane permeation, diffusion and gas sorption properties of carbon molecular sieve membranes derived from the prototype ladder polymer of intrinsic microporosity (PIM-1). *J. Membr. Sci.* **2016**, *504*, 133−140.

(26) Song, J.; Du, N.; Dai, Y.; Robertson, G. P.; Guiver, M. D.; Thomas, S.; Pinnau, I. Linear high molecular weight ladder polymers by optimized polycondensation of tetrahydroxytetramethylspirobisindane and 1,4-dicyanotetrafluorobenzene. *Macromolecules* **2008**, *41*, 7411−7417.

(27) Perez, E. V.; Balkus, K. J., Jr; Ferraris, J. P.; Musselman, I. H. Metal-organic polyhedra 18 mixed-matrix membranes for gas separation. *J. Membr. Sci.* **2014**, *463*, 82−93.

(28) Cheng, Y.; Ying, Y.; Japip, S.; Jiang, S.-D.; Chung, T.-S.; Zhang, S.; Zhao, D. Advanced porous materials in mixed-matrix membranes. *Adv. Mater.* **2018**, *30*, No. 1802401.

(29) Reid, B. D.; Ruiz-Treviño, F. A.; Musselman, I. H.; Balkus, K. J., Jr; Ferraris, J. P. Gas permeability properties of polysulfone membranes containing the mesoporous molecular sieve MCM-41. *Chem. Mater.* **2001**, *13*, 2366−2373.

(30) Koros, W. J.; Fleming, G. K. Membrane-based gas separation. *J. Membr. Sci.* **1993**, *83*, 1−80.

(31) Perez, E. V.; Kalaw, G. J. D.; Ferraris, J. P.; Balkus, K. J., Jr; Musselman, I. H. Amine-functionalized (Al) MIL-53/VTEC mixed-matrix membranes for H_2/CO_2 mixture separations at high pressure and high temperature. *J. Membr. Sci.* **2017**, *530*, 201−212.

(32) Furukawa, H.; Kim, J.; Plass, K. E.; Yaghi, O. M. Crystal structure, dissolution, and deposition of a 5 nm functionalized metal−

organic great rhombicuboctahedron. *J. Am. Chem. Soc.* **2006**, *128*, 8398−8399.
(33) Gill, P.; Moghadam, T. T.; Ranjbar, B. Differential scanning calorimetry techniques: applications in biology and nanoscience. *J. Bio. Tech.* **2010**, *21*, 167−193.
(34) Ryu, J.; Kim, H.-S.; Hahn, H. T. Reactive sintering of copper nanoparticles using intense pulsed light for printed electronics. *J. Electron. Mater.* **2011**, *40*, 42−50.
(35) Mott, D.; Galkowski, J.; Wang, L.; Luo, J.; Zhong, C.-J. Synthesis of size-controlled and shaped copper nanoparticles. *Langmuir* **2007**, *23*, 5740−5745.
(36) Yeshchenko, O. A.; Dmitruk, I. M.; Alexeenko, A. A.; Dmytruk, A. M. Size-dependent melting of spherical copper nanoparticles embedded in a silica matrix. *Phys. Rev. B* **2007**, *75*, No. 085434.
(37) Whitehead, C. B.; Özkar, S.; Finke, R. G. LaMer's 1950 model for particle formation of instantaneous nucleation and diffusion-controlled growth: A historical look at the model's origins, assumptions, equations, and underlying sulfur sol formation kinetics data. *Chem. Mater.* **2019**, *31*, 7116−7132.
(38) Ouyang, R.; Liu, J.-X.; Li, W.-X. Atomistic theory of Ostwald ripening and disintegration of supported metal particles under reaction conditions. *J. Am. Chem. Soc.* **2013**, *135*, 1760−1771.
(39) Ferrari, A. C.; Robertson, J. Raman spectroscopy of amorphous, nanostructured, diamond−like carbon, and nanodiamond. *Philos. Trans. R. Soc., A* **2004**, *362*, 2477−2512.
(40) Knight, D. S.; White, W. B. Characterization of diamond films by Raman spectroscopy. *J. Mater.* **2011**, *4*, 385−393.
(41) Tsaneva, V. N.; Kwapinski, W.; Teng, X.; Glowacki, B. A. Assessment of the structural evolution of carbons from microwave plasma natural gas reforming and biomass pyrolysis using Raman spectroscopy. *Carbon* **2014**, *80*, 617−628.
(42) Ferrari, A. C.; Robertson, J. Interpretation of Raman spectra of disordered and amorphous carbon. *Phys. Rev. B* **2000**, *61*, 14095.
(43) Robeson, L. M. The upper bound revisited. *J. Membr. Sci.* **2008**, *320*, 390−400.
(44) Behnia, N.; Pirouzfar, V. Effect of operating pressure and pyrolysis conditions on the performance of carbon membranes for CO_2/CH_4 and O_2/N_2 separation derived from polybenzimidazole/Matrimid and UIP-S precursor blends. *Polym. Bull.* **2018**, *75*, 4341−4358.
(45) Tin, P. S.; Chung, T.-S.; Liu, Y.; Wang, R. Separation of CO_2/CH_4 through carbon molecular sieve membranes derived from P84 polyimide. *Carbon* **2004**, *42*, 3123−3131.
(46) Shao, L.; Chung, T.-S.; Wensley, G.; Goh, S. H.; Pramoda, K. P. Casting solvent effects on morphologies, gas transport properties of a novel 6FDA/PMDA−TMMDA copolyimide membrane and its derived carbon membranes. *J. Membr. Sci.* **2004**, *244*, 77−87.
(47) Ogieglo, W.; Puspasari, T.; Ma, X.; Pinnau, I. Sub-100 nm carbon molecular sieve membranes from a polymer of intrinsic microporosity precursor: Physical aging and near-equilibrium gas separation properties. *J. Membr. Sci.* **2020**, *597*, No. 117752.
(48) Hays, S. S.; Sanyal, O.; Leon, N. E.; Arab, P.; Koros, W. J. Envisioned role of slit bypass pores in physical aging of carbon molecular sieve membranes. *Carbon* **2020**, *157*, 385−394.
(49) Kim, S.-J.; Lee, P. S.; Chang, J.-S.; Nam, S.-E.; Park, Y.-I. Preparation of carbon molecular sieve membranes on low-cost alumina hollow fibers for use in C_3H_6/C_3H_8 separation. *Sep. Purif. Technol.* **2018**, *194*, 443−450.
(50) Ma, X.; Williams, S.; Wei, X.; Kniep, J.; Lin, Y. S. Propylene/propane mixture separation characteristics and stability of carbon molecular sieve membranes. *Ind. Eng. Chem. Res.* **2015**, *54*, 9824−9831.
(51) Lozada-Hidalgo, M.; et al. Quantum tunneling of thermal protons through pristine graphene. *Science* **2016**, *351*, 68−70.
(52) Jiang, D. E.; Cooper, V. R.; Dai, S. Porous graphene as the ultimate membrane for gas separation. *Nano Lett.* **2009**, *9*, 4019−4024.
(53) Chi, C.; et al. Facile Preparation of Graphene Oxide Membranes for Gas Separation. *Chem. Mater.* **2016**, *28*, 2921−2927.
(54) Huang, S.; Dakhchoune, M.; Luo, W.; et al. Single-layer graphene membranes by crack-free transfer for gas mixture separation. *Nat. Commun.* **2018**, *9*, No. 2632.

https://doi.org/10.1021/acs.iecr.1c01727
Ind. Eng. Chem. Res. 2021, 60, 9962−9970